Preprint Cambridge Centre for Computational Chemical Engineering ISSN 1473 – 4273

Diradical aromatic soot precursors in flames

Jacob W. Martin[1,3,†], Laura Pascazio[3,†], Angiras Menon[1], Jethro Akroyd[1], Katharina Kaiser[4], Fabian Schulz[4], Mario Commodo[5], Andrea D'Anna[6], Leo Gross[4] and Markus Kraft[1,2,3]

released: 23 April 2021

[1] Department of Chemical Engineering and Biotechnology
University of Cambridge
West Site, Philippa Fawcett Drive
Cambridge, CB3 0AS
United Kingdom

[2] School of Chemical and Biomedical Engineering
Nanyang Technological University
62 Nanyang Drive
Singapore, 637459

[3] Cambridge Centre for Advanced Research and Education in Singapore (CARES)
CREATE Tower
1 Create Way, #05-05
Singapore, 138602

[4] IBM Research Zurich
Säumerstrasse 4
Rüschlikon, 8830
Switzerland

[5] Istituto di Scienze e Tecnologie per l'Energia e la Mobilità Sostenibile, CNR
P.le Tecchio 80
Napoli, 80125
Italy

[6] Dipartimento di Ingegneria Chimica, dei Materiali e della Produzione Industriale
Università degli Studi di Napoli Federico II
P.le Tecchio 80
Napoli, 80125
Italy

[†] Joint first authorship

Preprint No. 271

Keywords: soot formation, diradical, quantum molecular dynamics, localised π-radical, triplet ground state

Edited by
Computational Modelling Group
Department of Chemical Engineering and Biotechnology
University of Cambridge
West Site, Philippa Fawcett Drive
Cambridge, CB3 0AS
United Kingdom

Fax: + 44 (0)1223 334796
E-Mail: c4e@cam.ac.uk
World Wide Web: http://como.cheng.cam.ac.uk/

Abstract

Soot emitted from incomplete combustion of hydrocarbon fuels contributes to global warming [2] and causes human disease [24]. The mechanism by which soot nanoparticles form within hydrocarbon flames is still an unsolved problem in combustion science. Mechanisms proposed to date involving purely chemical growth are limited by slow reaction rates, whilst mechanisms relying on solely physical interactions between molecules are limited by weak intermolecular interactions that are unstable at flame temperatures [7, 55]. Here we show evidence for a reactive diradical aromatic soot precursor imaged using non-contact atomic force microscopy. Localisation of π-electrons on non-hexagonal rings was found to allow for Kekulè aromatic soot precursors to possess a triplet diradical ground states. Barrierless chain reactions are shown between these reactive sites, which provide thermally stable aromatic rim-linked hydrocarbons under flame conditions. Quantum molecular dynamics simulations demonstrate physical condensation of aromatics that survive for tens of picoseconds. Bound internal rotors then enable the reactive sites to find each other and become chemically crosslinked before dissociation. These species provide a rapid, thermally stable chain reaction toward soot nanoparticle formation and could provide molecular targets for limiting the emission of these toxic combustion products.

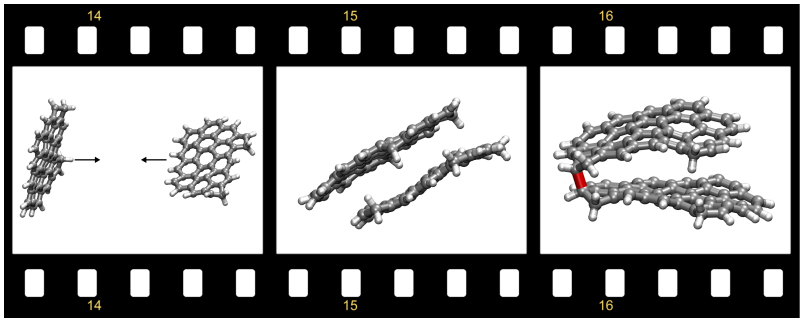

Highlights

- High resolution atomic force microscopy revealed species with localised π- monoradicals and π-diradicals.
- Thermally stable bonds were formed between diradicals enabling barrierless chain reactions to proceed.
- Collisons between π-diradicals were studied with quantum mechanical/molecular mechanics and internal rotors were found to enhance reaction efficiencies.

Contents

1 Introduction

Soot emitted into the atmosphere contributes to global warming and when deposited on ice soot lowers its albedo, increasing melting [2]. Recent estimates place the atmospheric radiative forcing of black carbon at 0.5–1.0 W/m^2, similar to that of methane [2]. Additionally, soot and other < 2.5 μm combustion products ($PM_{2.5}$) have been directly correlated with increased morbidity and respiratory diseases [24]. Most pressing is preliminary evidence that an increase of only 1 μm/m^3 of $PM_{2.5}$ in the urban environment is associated with an 11% increase in COVID-19 related deaths (in preliminary data from the USA) [56]. Recent lockdown measures also demonstrated how quickly soot emissions can drop in the atmosphere with a 12% reduction in $PM_{2.5}$ emissions in 50 major cities around the world, indicating that air quality can rapidly recover [43]. Formation of carbonaceous aerosols are not limited to earth but litter our universe as interstellar dust and are found in the atmospheres of planets and moons, such as Titan [25].

No predictive model yet exists for carbonaceous nanoparticle formation, inhibiting our ability to eliminate these pollutants from combustion systems [22]. The critical transformation is inception (or nucleation) where gas phase aromatic soot precursors cluster to form nanoparticles (see Figure 1). Three main requirements have been found for this transformation: 1) The species involved must sustain a chain reaction where reactivity or condensability is maintained through subsequent monomer additions [7, 20]; 2) The molecules must be thermally stable with bond energies or intermolecular energies in excess of approximately –167 kJ/mol required for thermal stability at temperatures in the flame where soot begins to form (>1500 K) [31, 53, 55]; 3) High collision efficiencies are required to explain the rapid formation of nanoparticles in flames [7]. To date, no soot precursor has been found that is able to achieve these three requirements.

Electron paramagnetic resonance spectroscopy demonstrates that π-radicals are dominant in early soot nanoparticles and appear to be critical in their inception [54]. π-electrons are delocalised in aromatic species that contain six-membered rings and are therefore unreactive [38]. Localisation of π-radicals has long been suggested to provide increased reactivity [1, 23, 55, 57]. The last decade has seen significant work on aromatics with ex-

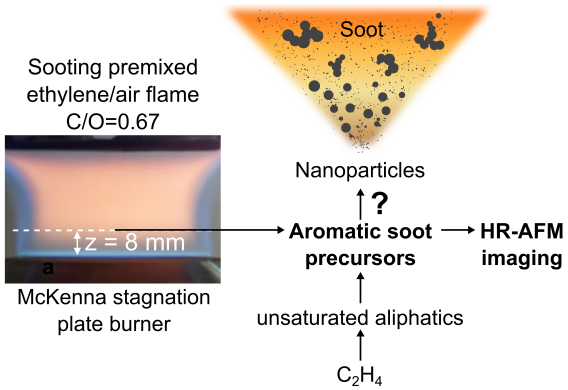

Figure 1: ***Aromatic soot precursor collection****. Burner configuration, collection location and schematic of soot formation.*

tended zig-zag edges, such as acenes, which have been shown to localise π-electrons and crosslink [23, 55, 57]. However, few of these extended zig-zag edges are seen in flame aromatics [5] and the crosslinks are not expected to be thermally stable in a flame [33]. Recent images of the aromatic molecules in flames have revealed partially saturated edges on aromatic molecules [5]. Using electronic structure theory we demonstrated that these partially saturated edges form highly localised π-radicals [31, 33], which were initially hypothesed by Abrahamson in 1977 [1]. Of interest for formation mechanisms, localisation of π-electrons were found to allow for multiple reactive sites on a single aromatic molecule (with the simplest being a diradical) [34], which is a requirement for sustaining a chain reaction. Spectroscopic measurements of these radicals have been undertaken in the astrochemistry community, with their fluorescence suggested to be involved in the unidentified emission from the Red Rectangle proto-planetary nebula [41].

In this letter, an aromatic soot precursor imaged with high resolution atomic force microscopy is found to possess a triplet diradical ground state. Localisation of π-electrons on non-hexagonal rings is found to be required for this Kekulé aromatic to form the high spin ground state. These species allow for barrierless reactions with thermally stable bonds capable of a chain reaction. Finally, quantum molecular dynamics simulations reveal rapid reactions between diradical soot precursors, enabled by internal rotors.

2 Methods

2.1 Non-contact atomic force microscopy

Details of the sampling and imaging of the flame aromatics can be found in previous publications [5, 47]. Briefly, combustion products were sampled from a sooting laminar premixed flat flame (see Figure 1) and collected on a quartz filter for 14 hrs. We used a home built STM/AFM setup operating in ultra-high vacuum and at low temperature ($T =$ 5 K). Flash heating was used to deposit the aromatic soot precursors onto the substrate. A qPlus quartz cantilever [12] was operated in frequency modulation mode with a carbon monoxide functionalised tip [13]. The AFM images are recorded at constant height, at $V = 0$ V bias voltage. The resonance frequency was $f_0 = 28.8$ kHz, the quality factor $Q \sim 100,000$, and we used an oscillation amplitude of $A = 50$ pm. To facilitate structure assignment, several AFM images at different tip-molecule distances where acquired for a given molecule and, if accessible, also images of the frontier orbitals densities by STM (see Supplementary Information). Comparison between the species found in AFM with Raman analysis and mass spectrometry confirm they are representative of the species found in the gas phase [44, 47].

2.2 Electronic structure calculations

The collection of molecules were geometry optimised using the hybrid density functional theory B3LYP/6-311G(d,p). Molecular energies were calculated using the hybrid meta-GGA DFT method M06-2X/cc-pVTZ in the software Gaussian 16 [10]. This level of the-

ory has been found to provide molecular energies to within 10 kJ/mol of experiments [58] and accurately reproduced bond energies to within 8 kJ/mol to experimentally derived values and reaction rates between aromatic radicals to within an order of magnitude [34]. Singlet-triplet energy was calculated using the geometries from B3LYP/6-311G(d,p) and the DLPNO-CCSD(T)/cc-pVTZ method in the software ORCA [39], which is known to accurately reproduce energies and singlet-triplet gaps to within 3 kJ/mol at this level of theory [11]. The T1 diagnostic was found to be below 0.2 in all cases indicating a single spin configuration is appropriate.

2.3 Molecular dynamics

A dynamic study on the dimerisation of π-radicals under flame conditions is performed using mixed classical molecular mechanics (MM), also known as molecular dynamics, simulations and quantum mechanics/molecular mechanics (QM/MM) simulations. A series of homobinary collisions between the π-radicals is performed with classical MM simulations. Before studying the binary collisions, structural equilibrium of PAH radicals was performed in the canonical ensemble (NVT) at temperatures of 1500 K. Constant temperature is maintained by a chain of Nosé-Hoover thermostats with a damping constant of 200 fs. Afterwards, binary collisions between PAH radicals are performed in the canonical ensemble (NVT) with a time step of 1 fs. To achieve statistical significance, a total of 1000 binary collisions are performed for each case. The initial relative centre of mass distance between the two colliding PAH molecules/radicals was 30 Å, which is larger than the effective intermolecular interaction distance between PAHs. The relative translational velocities are set equal to the average speed in the Maxwell-Boltzmann distribution at 1500 K. The orientation of the starting molecules is randomly sampled in three axes. The classical MM simulations are performed using GROMACS. The intramolecular interactions are described using the OPLS-AA force field. The dispersion interactions are described by the isoPAHAP force field based on benchmark SAPT(DFT) calculations [53]. This force field has been successfully applied to investigate the clustering of aromatic species and accuracy reproduces the virial coefficient of benzene. The distance between two reactive sites is then tracked during the whole simulation. When the two reactive sites are at a distance lower than 3 Å the simulation is switched to QM/MM to determine whether a bond forms between the reactive sites. The QM/MM simulations are performed using GROMACS coupled with ORCA software. The reacting parts of the system are treated quantum mechanically, with the remainder being modelled using the force field (see Supplementary Information). The interactions between the QM and MM subsystems are handled within the ONIOM approach. Twelve different monomers have been selected with different sizes and radical types. The quantum mechanical region consists of the pentagonal rings and the adjacent hexagonal rings for the two π-radical site types and the hexagonal ring for the σ-radical (see Supplementary Information). The broken symmetry unrestricted method (BS-UM06-2X/def2-SVP) is employed to simulate the QM regions with correct dissociation dynamics.

3 Results and discussion

Non-contact atomic force microscopy (nc-AFM) revealed a variety of aromatic soot precursors with localised electronic states. Figure 2a shows a coronene structural motif with two rim-based pentagonal rings, one of which is partially saturated, named **1** in this paper (the partial saturation has been confirmed with further imaging and negative ion resonance imaging see Supplementary Information). We have recently demonstrated that a significant concentration of these sites are expected in the flame as hydrogen is added and abstracted from the pentagonal rings' edges (*i.e.* being in partial equilibrium with $H^{\cdot}/H_2$) [34]. Figure 2b shows the electron spin density determined from electronic structure calculations revealling the presence of a doublet localised π-radical. This is seen from their spin density which does not decrease with increasing size, showing pinned electronic edge states (a variety of other non-hexagonal rings and methylene type species are also shown to be localised in the Supplementary Information). Therefore, while these states are resonantly stabilised, with spin density shared among multiple aromatic carbons, they are localised to the edge, maintaining their spin density and therefore high reactivity with enlargement.

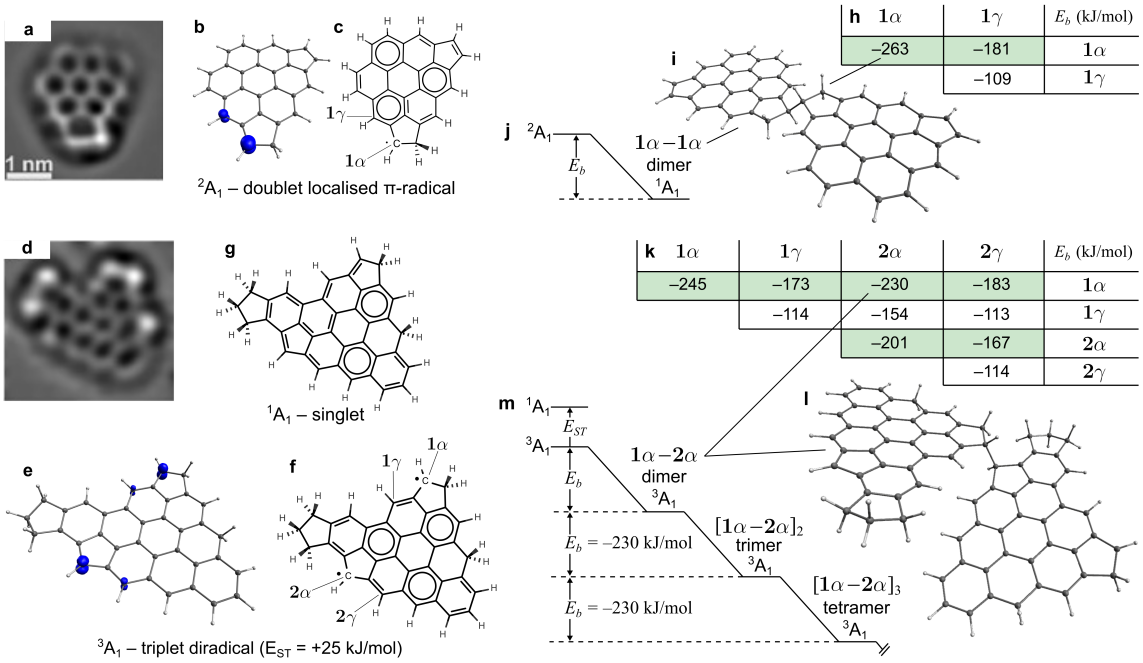

Figure 2: ***Imaging, electronic structure and reactions of aromatic radicals.*** *a) & d) HR-AFM images of aromatic soot precursor species (Laplace-filtered sharing the same scale shown in a)). b) & e) spin density surfaces (iso=0.025 a.u.) for the electronic ground state. c), g) & f) the dominant Kekulé structures are also shown. h) & k) The bond energy E_b in kJ/mol is shown for each crosslink. i) & l) Shows the geometries of one such crosslink. j) & m) Reaction mechanisms for the doublet monoradical and the triplet diradical with the later allowing subsequent polymerisation with no loss in reactivity.*

Imaging with nc-AFM also suggests that the molecule shown in Figure 2d) is present in the flame. This molecule features a partially protonated rim-based pentagonal ring and embedded pentagonal ring, labelled **1** and **2**, respectively in Fig. 2f) (the structural assignments are discussed in detail in the Supplementary Information). Of significance to soot formation, this species was computed to possesses a ground state that is a triplet ($E_{\mathrm{ST}} > 0$). The energy gap between the singlet and triplet states, E_{ST}, provides a reliable metric for diradical character [49], where $E_{\mathrm{ST}} \rightarrow 0$ suggests an increasing diradical character (diradicaloid) and $E > 0$ indicates a true diradical with a triplet ground state. Some well known diradicaloids, those that contain diradical-character, were also found in the flame, including pentacene (protonated in the imaging) and p-quinodimethane (see Supplementary Information). It has been found for p-quinodimethane that thermal excitation of this species into its triplet state allows for a chain polymerisation reaction to proceed in the condensed phase [18, 49]. However, this species is the first evidence of a species that is a true diradical with high spin ground state. Figure 2e) shows the electron density and Kekulé of this state with spin density concentrated at the rim in a similar configuration to the doublet.

This diradical aromatic is uncommon in that it is a high-spin Kekulé aromatic. A Kekulé aromatic possesses a chemical structure where each aromatic carbon has a valence of 3 from a combination of single and double bonds see Fig. 2g). Kekulé aromatic species composed of six-membered rings have only been found to possess a singlet ground state and can only attain a triplet ground state for a non-Kekulé configuration of rings (*e.g.* the recently synthesised heptauthrene [50] and the extended triangulenes [26, 37]). The stabilisation of high-spin ground states in Kekulé aromatic has recently been demonstrated in synthesised nanographene structures with two fluorene-like moities [27]. These high-spin ground states in Kekulé aromatics demonstrate that truly localised states can exist due to topological defects *i.e.* non-hexagonal rings [49]. (Further details concerning the role of aromaticity in stabilising the high-spin ground state can also be found in the Supplementary Information.)

The reactivity and thermal stability of crosslinks formed between the localised π-radicals shown in Figure 2d) are computed with electronic structure theory. Figure 2 shows the computed bond energies for the possible crosslinks between sites **1** and **2** denoting the partially saturated rim-based pentagonal ring-type (*e.g.* acenapythenyl) and fluorenyl-type edges, respectively, where the α and γ carbon atoms are the most spin-rich and reactive (see Fig. 2c) and f)). The unstacked configurations were chosen to provide the best comparison between site reactivities without interference from the dispersion interactions in the overlapping geometries [31]. As mentioned, it has been found experimentally that bonds lower than approximately 167 kJ/mol in magnitude are rapidly degraded in hydrocarbon flames [31, 55]. This cut-off provides various possible configurations of interest (labelled in green in Fig. 2). The strongest bonds formed were between $\mathbf{1}\alpha$–$\mathbf{1}\alpha$ sites (with the geometry most closely related to 1,1',2,2'-Tetrahydro-1,1'-biacenaphthylene), $\mathbf{2}\alpha$–$\mathbf{2}\alpha$ (with a geometry most closely related to 9,9'-Bifluorene) and $\mathbf{1}\alpha$–$\mathbf{2}\alpha$ with approximately half the bond strength of the C–C single bond in ethane but double that of a bond between two π-radicals on six-membered rings [38]. Reactions between the γ sites were not found to be thermally stable in the flame but may be important after soot has condensed. Minimal differences are found between the bond energy between the $\mathbf{1}\alpha$ site for the mono- and diradicals ($\approx$5%), or with the smaller acenapythenyl dimer we have previously cal-

culated [31] ($\approx 1.5\%$), showing that reactivity is not dependent on neighbouring radicals nor on the size of the aromatic strongly suggesting edge localisation. Figure 2 b) shows the polymerisation of the **1**α–**2**α sites. Critically, after two triplet π-diradicals (^3A_a) form a dimer involving their α sites the triplet state endures allowing for further barrierless reactions to occur. We confirmed that for the **1**α–**2**α reactions the bond energy for the dimer + monomer $\rightarrow$ trimer and subsequently the tetramer provide the same bond energy of 230 kJ/mol (we also confirmed the bonds are thermodynamically favoured at flame temperatures see Supplementary Information). These reactions therefore can proceed in a chain reaction with no reduction in reactivity, which we call polymersisation of aromatic rim-linked hydrocarbons (PARLH).

Quantum molecular dynamics is used to study the reaction dynamics for a variety of recombining localised π-radicals and σ-radicals found in the flame. Figure 3a) and b) shows some π-diradicals that were theoretically prepared from hydrogen abstraction (a common reaction in the flame [34]) of species observed in nc-AFM [5] (the triplet ground states are demonstrated for these species in the Supplementary Information). The σ-radicals are involved in the extension of the aromatic domains with acetylene [7] and have been suggested to be involved in many soot inception mechanisms [6, 7, 35]. Figure 3c) shows the fraction of effective collisions, $F_{\text{reac.}}$, where a bond is formed during the collision and provides a means of suggesting possible trends in the collision efficiency (see Supplementary Information for implementation and comparison with radical recombination rates and Supplementary Movie 1 for a representative collision between the diradical in Figure 2e)). As σ-radicals enlarge their $F_{\text{reac.}}$ reduces, which has been previously demonstrated with reactive molecular dynamics [29]. σ-diradicals are found to provide a modest enhancement in the reactivity over the monoradical. For π-radicals the opposite trend is found with increasing molecular enlargement – $F_{\text{reac.}}$ increases, significantly so for π-diradicals.

To explore the reason for this enhancement the largest π- and σ-diradical species, shown in Figure 3m) and f) respectively, are compared. Supplementary Movie 2 shows a representative trajectory for the σ-diradical, where the bond forms upon initial collision. Supplementary Movie 3 shows a σ-diradical forming during dissociation, which happens less frequently. Both Supplementary Movie 2 & 3 show the bond formed when the two molecules are not stacked but when the aromatic planes are close to collinear. In fact trajectories were found where the molecules were stacked for an extended time with the reactive sites frequency approach each other, however, no bonds were formed when the aromatics were stacked (see Supplementary Movie 4). This follows from the orthogonality constraints on the sp^2 hybridised σ-radicals where the orbitals maximally overlap when the carbon atoms are collinear with the aromatic planes.

The dynamics are significantly more complex between two π-diradicals and therefore we considered a larger species (see Supplementary Movie 5) and computed some timeseries metrics to aid with the analysis. Figure 3n) shows the distances between the centres of mass for the fragments as well as between the reactive sites. The distance between centres of mass indicates whether or not the aromatic planes are stacking and physically interacting before the bond is formed. Significant modulation in the distance between the reactive sites is seen before the bond is formed at 41.5 ps and the length is constrained. To further explore this the angle between the reactive sites is computed in Figure 3o). The reactive sites are found to follow a sinusoidal pattern demonstrating a stably bound

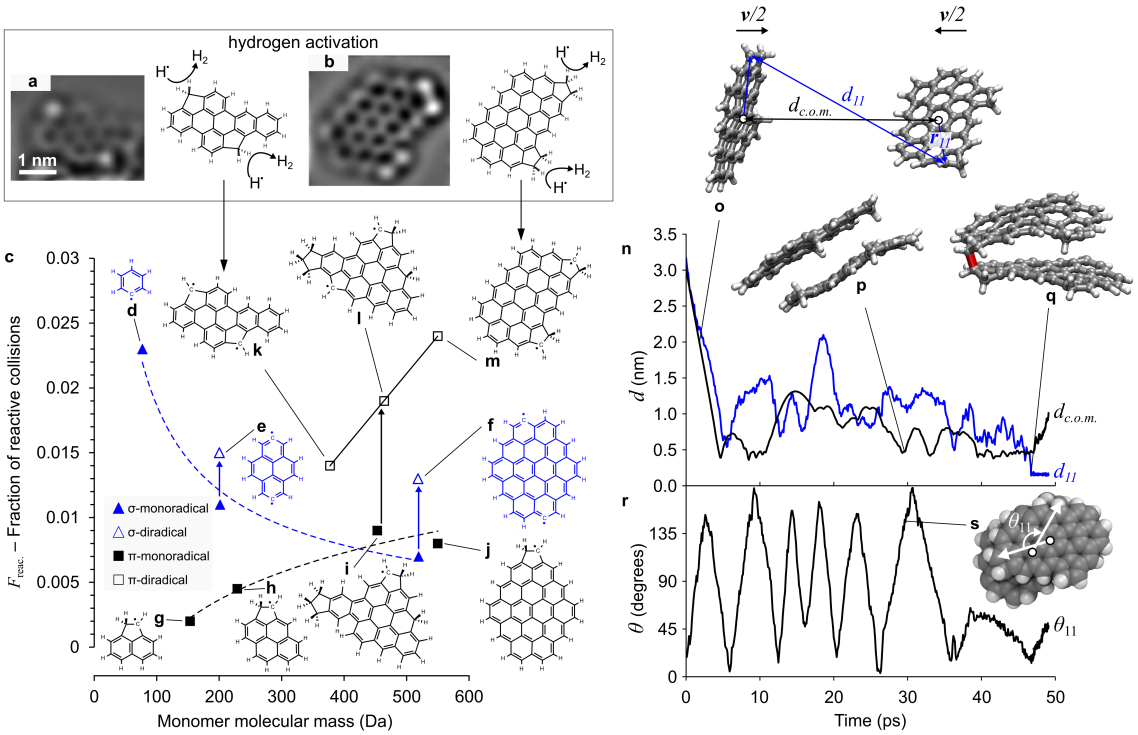

Figure 3: ***Radical recombination of aromatic radicals.*** *a) and b) Formation of diradicals from hydrogen abstraction of species imaged with nc-AFM from Commodo et al.[5]. c) Fraction of effective reactive collisions determined using QM/MM simulations for d–f) σ-monoradicals and σ-diradicals with filled and open triangle symbols, respectively. g-j) π-monoradicals filled square symbols. k-m) π-diradicals open square symbols derived from HR-AFM structures [5]. n) A single reactive trajectory is shown for the diradical in m). o) Distances between the centres of mass ($d_{C.O.M.}$) and the reactive sites that bond, d_{11}, are plotted. o–q) Insets shows the geometries of the o) species approaching, p) stacking unbonded and q) stacking and bonding. r) Angle, θ_{11}, between the vectors, $\boldsymbol{r}_{11}$, from the centre of mass to the reactive sites (see o)) show the rotation preceding the bond formation. s) Inset shows a different orientation of the p) geometry with the direction of rotation in the plane of the aromatic highlighted.*

internal rotor is present. In this trajectory, internal rotors allow the reactive sites to find each other and bond before the molecules dissociate. Supplementary Figure S10 compares the dissociation times for this species with the large σ-diradical. They are found to possess similar dissociation lifetimes due to many collisions leading to a physically bound dimer. We can then consider the fraction of collisions where the reactive sites approach each other, $F_{\text{appr.}}(r_{\text{cutoff}} < 0.3\ nm)$. For the σ-diradical this fraction is almost double that of the π-diradical, most likely due to the steric issues associated with the saturated carbon site in the latter case. However, the fraction of reactive collisions, $F_{\text{reac.}}$, resulting in a bond forming the π-diradical is approximately double that of the σ-diradical, suggesting the increased lifetime of the dimer enhances the reactions only between π-radicals due to a physically bound internal rotor. Supplementary Figure S11 shows that this trend is seen

for all species where the dissociation time increases with molecular size while only for the π-radicals is a positive correlation found between the fraction of effective collisions and the dissociation lifetime. It should also be mentioned that reactive collisions were only considered between the most reactive α sites and therefore these simulations are an underestimates and only capture the most significant reactions. More work is required to compute the collision efficiency using more cost-effective methods. Electrostatic effects may also enhance the clustering if polar curved aromatics possess these reactive sites, particularly for interactions with charged chemi-ions which also need to be explored [30].

Frenklach and Mebel recently suggested an enhancement due to internal rotors for chemical mechanisms involving small aromatic molecules, which are too slow to provide the nucleation flux experimentally seen [7]. These quantum molecular dynamics simulations provide the first evidence for such an enhancement, which is significant for localised π-radicals and can lead to highly efficient reactions approaching that of species that are known to rapidly recombine in the flame such as phenyl [15]. Preliminary experimental evidence for such a mechanism has been seen for benzyl recombination [28]. For this smallest localised π-radical a rapid reaction rate was found that surpassed the high pressure limit when nearing its vapour point where physical interactions become important.

To fully assess localised π-multiradicals as potential soot precursors, their concentration in the flame must also be determined. Our preliminary computational study of rim-based pentagons (acenapthlyene-type) in partial equilibrium with $H^{\cdot}/H_2$ in the flame revealed that diradicals can form in significant concentrations if multiple rim-based pentagonal rings are present [34]. Similar analysis is required for the variety of localised π-radical types highlighted in this paper. Another interesting observation is that due to the resonance stability of localised π-radicals, their reaction with molecular oxygen has been shown to be slow at flame temperatures (*e.g.* for benzyl [40]), suggesting their concentration could grow as does propargyl (known to be the primary route to benzene [15]) for the same reason. Atomic oxygen, which can be added via ozone addition, has been found to react readily with fluorenyl-type localised π-radicals [9] and could provide a potential route to eliminating these sites in flames. Preliminary evidence suggests significant reduction in soot formation with ozone injection [51].

4 Conclusions

In conclusion, we have shown evidence for a triplet π-diradical that is able to fulfill many of the requirements for carbonaceous nanoparticle formation by; providing a chain reaction, bonding strongly enough for stability at flame temperatures and reacting rapidly through physically stabilised internal rotors. These results provide evidence for a pathway involving both chemical and physical interactions of aromatic radicals, long sought in soot formation research [1, 7, 8, 16, 21, 36] and most clearly articulated, perhaps, in 1989 by Harris and Weiner: "Once coagulated they will quickly become chemically knit together since a significant fraction of the aromatic species are radicals" [16].

Acknowledgments

This project is supported by the National Research Foundation (NRF), Prime Minister's Office, Singapore under its Campus for Research Excellence and Technological Enterprise (CREATE) programme. The authors are grateful to EPSRC (grant number: EP/R029369/1) and ARCHER for financial and computational support as a part of their funding to the UK Consortium on Turbulent Reacting Flows (www.ukctrf.com). AM gratefully acknowledges Johnson Matthey for financial support. MK gratefully acknowledges the support of the Alexander von Humboldt Foundation.

Supplementary Data

Supplementary Movies 1-5 for representative collisions are provided via the University of Cambridge data repository (https://doi.org/10.17863/CAM.68556) and can also be provided upon request.

A Supplementary Material

A.1 High resolution atomic force microscopy

Extended discussions on the imaging approach can be found in our previous publications and in the main text [5, 47]. We conducted additional analysis on the structural elucidation of the species discussed in the main text. In particular, the differentiation of CH and CH_2 moieties at the edges of the molecules at five-membered rings is challenging and is analyzed and discussed here in detail.

Figure S1 shows extended scanning tunnelling microscopy (STM), density functional theory (DFT) and atomic force microscopy (AFM) data on the first species, labelled IS1 in previous work [5], which was imaged on bilayer NaCl on Cu(111) with a CO functionalized tip. With constant current STM at an applied sample bias $V = 0.2$ V, which is within the transport gap of the molecule, electrons cannot be attached to the molecule and the image contrast is explained by a lowering of the tunnelling barrier for the path through the molecule [42], revealing little intramolecular contrast, see Fig. S1a.

With STM at $V = +1.7$ V, see Fig. S1b, we could access the negative ion resonance (NIR) of this molecule. At this bias, we attach from the tip, electrons to the first unoccupied state above the Fermi level, *i.e.*, the lowest unoccupied molecular orbital (LUMO). The constant current STM image at resonance can be interpreted as a contour map of the corresponding orbital density [42]. In addition, the usage of a CO functionalized tip gives

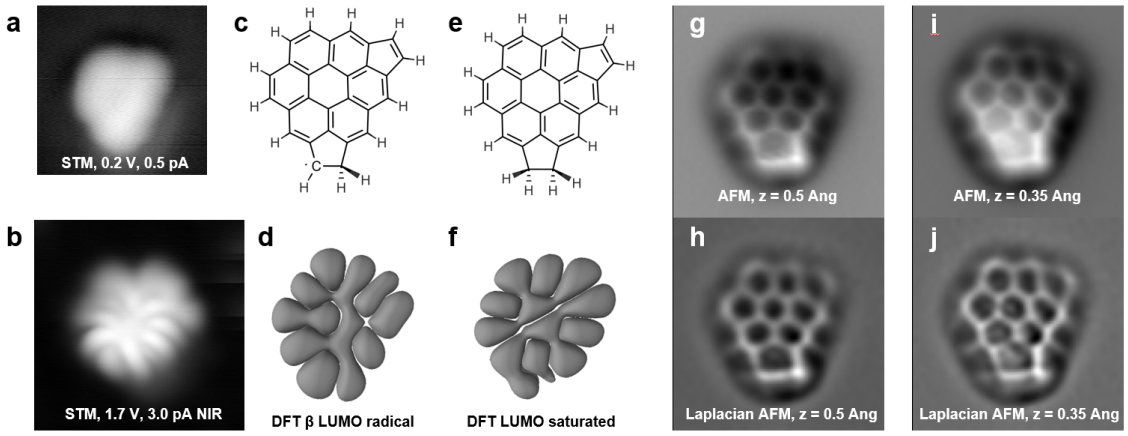

Figure S1: *Additional STM, DFT and AFM data for IS1. STM images of at (a) $V = 0.2$ V, $I = 0.5$ pA and (b) $V = 1.7$ V, $I = 3.0$ pA on bilayer NaCl on Cu(111) using a CO functionalised tip. Structure (c) and calculated LUMO density at an iso-surface value of 0.002 of IS1 (d). Structure of a molecule featuring a second CH_2 moiety at the five-membered ring of IS1, resulting in a closed shell structure (e) and its calculated LUMO density (f). Constant height AFM data at different tip height z is shown in (g) and (i), together with the corresponding Laplace filtered images (h) and (j), respectively. A decrease in z corresponds to a decrease in tip-sample distance.*

rise to a partial p-wave character of the tip, with sensitivity to the lateral gradient of the orbital densitt [14].

We calculated the LUMO at the M06-2X/cc-pVTZ level of theory for the previously assigned molecular structure IS1 [5, 47]. The structure of the molecule is shown in Fig. S1c and the calculated LUMO orbital density (in this case, as the molecule is a radical, corresponding to a singly unoccupied molecular orbital) at an iso-surface value of 0.002 is shown in Fig. S1d. In Addition, we also calculated the LUMO for a closed shell molecule that features a second CH_2 moiety at the five-membered ring, see its structure shown in Fig. S1e and its calculated LUMO iso-surface in Fig. S1f.

The calculated LUMO density of the radical IS1 (Fig. S1d) fits very well the STM measurement (Fig. S1b), whereas the LUMO of the closed shell structure molecule with an additional CH_2 moiety (Fig. S1f) does not. This electronic characterization by STM and its comparison with the calculated orbital densities firmly corroborates our structural assignment of IS1 of the previous publication [5].

This molecule showcases the challenge in assigning that specific moiety, *i.e.*, the level of saturation of the five-membered ring with a CH_2 moiety. At the position of the CH group in that five-membered ring, the AFM contrast is significantly brighter compared to the contrast on the other CH groups within the molecule (see Fig. S1g and Fig. S1i). This increase in brightness could be explained by a non-planar adsorption geometry, and increased adsorption height at the CH group at the five-membered ring, caused by the neighboring CH_2 moiety, leading to a locally increased adsorption height and tilted adsorption plane of the molecule [45].

Figure S2 shows additional AFM and STM data that was measured on molecule IS56 on bilayer NaCl on Cu(111). Unfortunately, we did not acquire STM images at ionic resonance for that molecule, because the molecule was picked up by the tip before or-

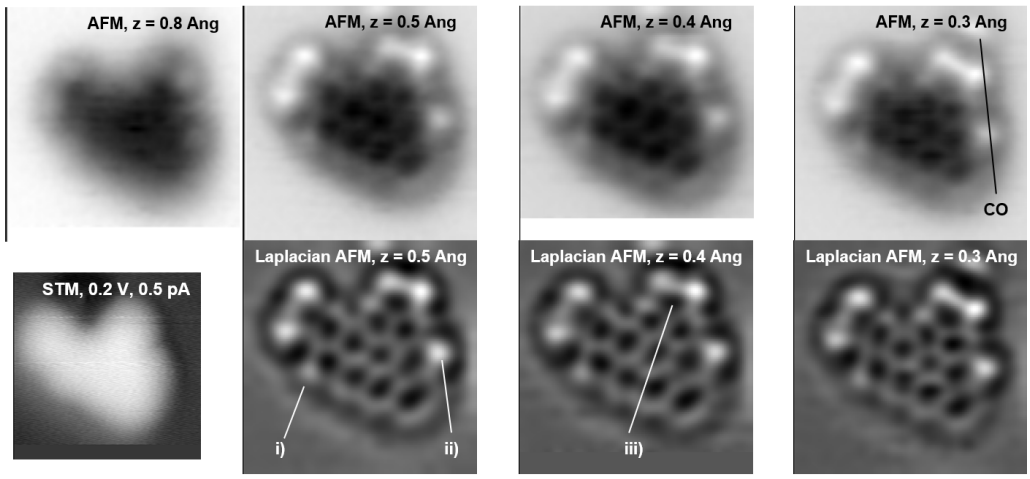

Figure S2: *Additional STM and AFM data for IS56. Constant current STM in gap image at $V = 0.2$ V, $I = 0.5$ pA on bilayer NaCl on Cu(111) using a CO functionalised tip, labelled STM. Constant height AFM data at different tip height z together with the corresponding Laplace filtered images. A decrease in z corresponds to a decrease in tip-sample distance.*

bital density images were obtained. AFM images of the molecule are shown for different tip heights in Fig. S2. The aliphatic six-membered ring is assigned in comparison with ref. [46] with high confidence. The CH group at a five-membered ring labelled i) and the CH_2 group at a six-membered ring labelled ii) in Fig. S2 are assigned with high confidence, too. More challenging and of less confidence is the assignment of the saturation of the five-membered ring labelled iii) in Fig. S2. Comparison to molecule IS1, that features a very similar AFM contrast, indicates that this is likely a partially saturated five-membered ring, i.e., with one CH and one CH_2 moiety, as in IS1, suggesting the initially proposed structure IS56 [5]. However, we cannot firmly exclude a five-membered ring with two CH_2 groups, as we are missing STM orbital density images to confirm this challenging structural assignment for this molecule, in contrast to IS1. In the context of this work it is important to note that both possible assignments for this molecule, *i.e.*, IS56 and the hydrogenated radical of IS56 with two CH_2 groups at the five-membered ring, could be interconverted by exchange of atomic hydrogen in the flame [5]. Thus, both possible structural assignments suggest that both molecule IS56 and the hydrogenated radical of IS56 are present in the flame.

A.2 Localisation of Π-radicals

The localisation of π-radicals can be demonstrated from the spin density for a variety of aromatic radicals with a doublet ground state. Figure S3 shows the isosurface of the spin density calculated for a variety of motifs as a function of molecular size. The spin density is correlated with the resulting reactivity of the carbon atom [49]. We have previously demonstrated the distinction between the delocalised π-radicals (phenalenyl-type) and localised π-radicals for the partially saturated rim pentagon-type (Part. sat. rim pent-type) [31], however, based on the saturated edges found via non-contact AFM [5] other

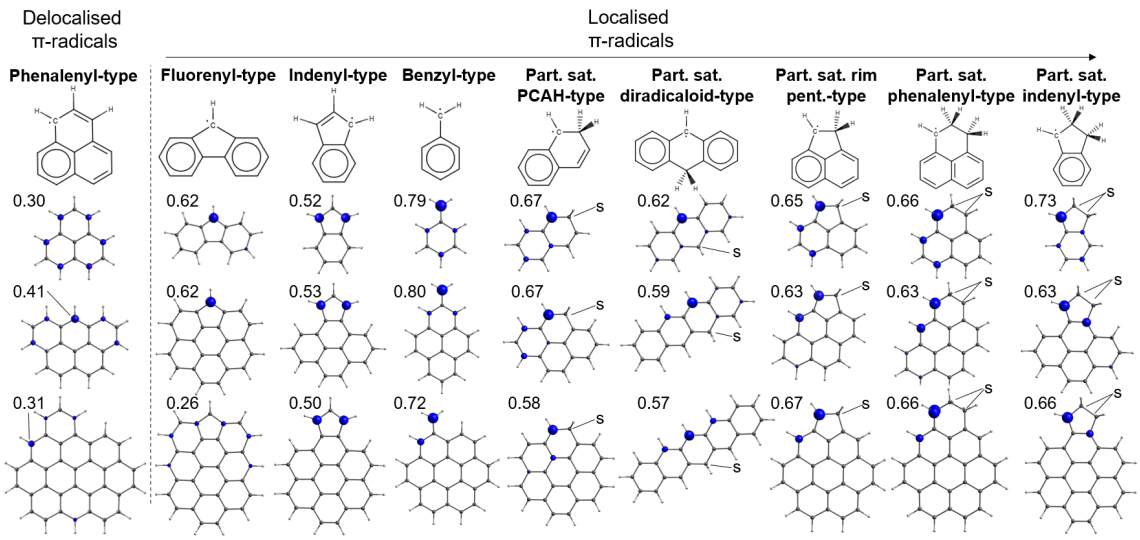

Figure S3: *Spin density (iso=0.025) study of delocalised versus localised π-radicals as a function of molecular size. The Mullikan spin is also shown for the most spin-rich carbon atom.*

localised π-radicals could be generated from hydrogen addition/abstraction. For benzyl-type radicals these sites have also been referred to as α-radicals due to the concentration of spin density on a primary α-carbon atom [4]. They arise from aromatics that contain non-hexagonal rings, methylene groups or zig-zag edges.

A more concrete definition of localisation has been proposed recently based on aromatic diradicals [49]. The singlet-triplet energy, E_{ST}, is described as a measure of the diradical character. A variety of imaged molecules were found to have diradical character, diradicaloids, with $E_{ST} < 0$ and $E_{ST} \to 0$ (see Fig. S4). For species for which a triplet ground state is found, where $E_{ST} > 0$, these are considered to be localisable states [49]. For aromatic molecules only containing hexagonal ring networks this has only been achieved for non-Kekulé aromatics, however, the species imaged in the main text are all Kekulé aromatics as can be seen from Fig. S4. The stabilisation of the high spin state in these aromatics provides more evidence that these reactive sites as electronically localised and

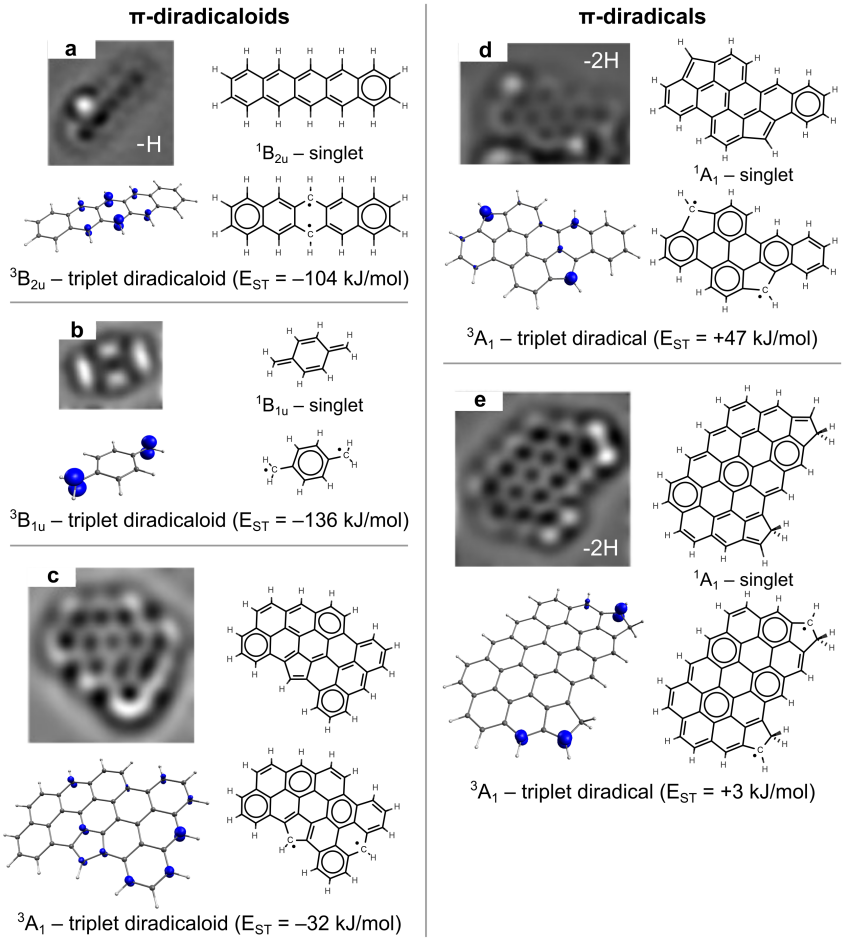

Figure S4: *nc-AFM imaging and electronic structure analysis of π-diradicaloids and π-diradicals. For species a), d) and e) hydrogen was removed from the imaged molecule to provide the diradical(oid) species. Singlet-Triplet energy gaps, E_{ST} are provided to determine diradical character at the DLPNO-CCSD(T)/cc-pVTZ//B3LYP/6-311G(d,p) level of theory.*

is related to their aromaticity [49].

The Clar construction provides an analysis of the degree of aromatic stabilisation. Sextets (six-membered rings can contain 6 π-electrons that are in resonance) are drawn with a circle and indicate resonantly stabilised 6-member cycles, with more sextets indicating greater stability [48]. Figure S4 reveals that while closed shell Kekulé structures can be drawn for many of these molecules, the open-shell structure often contains more Clar sextets indicating greater aromatic stability is involved. We have previously used such an analysis to argue for the localisation of the π-radical in the doublet state [34] but it appears a similar effect enables diradical states to be stabilised on aromatic species.

Another indication of localisation is the sustained bond strength as a polymer is constructed. Figure S5a-c shows the dimer, trimer and tetramer geometries for the **1**α–**2**α series. The binding energy for the addition of one monomer were all found to be –230 kJ/mol for the dimer, trimer and tetramer showing no loss of reactivity. This indicates that the reactivity of one reactive site does not depend on the bonding state of the other reactive site showing the localisation of the reactivity.

Finally, a question arises as to whether these crosslinks are thermally stable from a thermodynamics point of view. Figure S5d shows the equilibrium analysis for the dimerisation of two monomers of **1**α–**2**α. Full vibrational analysis of the monomers and dimers as well as the energetics were computed, allowing for the temperature dependent equilibrium constant for dimerisation to be computed. We find a positive value over the entire range of temperatures seen in hydrocarbon flames (<2500 K). This suggests that once the crosslinks are formed they will be persistent and thermally stable. This result is consistent with our previous calculations on smaller localised π-radical species [33].

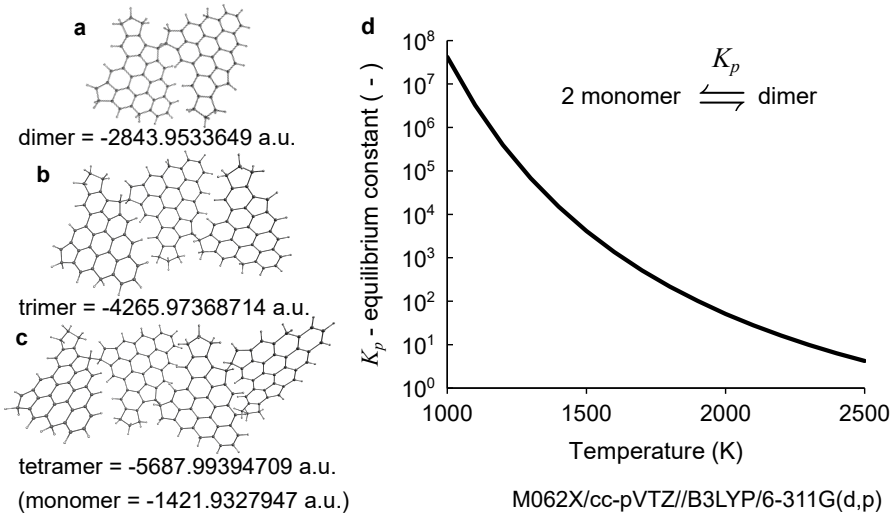

Figure S5: *a-c) Geometries and energies for the dimer, trimer and tetramer. d) Equilibrium constant for dimerisation is computed for the* ***1***α*–****2***α *dimer showing that the product is favoured at temperatures found in the flame.*

A.3 Quantum Mechanics Molecular Mechanics simulations

In this work, the crosslinking reactions have been simulated using a combination of quantum mechanics (QM) and molecular mechanics (MM). The reactive sites are treated quantum mechanically, with the remainder being modeled using the iso-PAHAP force field for the intermolecular interactions and OPLS-AA force field for the intramolecular interactions. The QM/MM division connects the systems along chemical bonds (see Fig. S6). At the bonds that connects the QM and MM subsystems, link atoms are introduced (labelled LA in Fig. S6). These link atoms are present as a hydrogen atom in the QM calculation step and are not physically present in the MM subsystem, but the forces on it are computed in the QM step and are distributed over the two atoms in the bond as will be discussed. The QM region is simulated with ORCA software using broken symmetry spin unrestricted SCF calculations (BS-M06-2X/def2-SVP). Molecules with three different types of reactive sites are simulated: a σ-radical and two π-radical site types - partially saturated rim pentagon type (defined as $\mathbf{1}\alpha$ in Fig. 2g) and fluorenyl type (defined as $\mathbf{2}\alpha$ in Fig. 2g) - (Fig. S6).

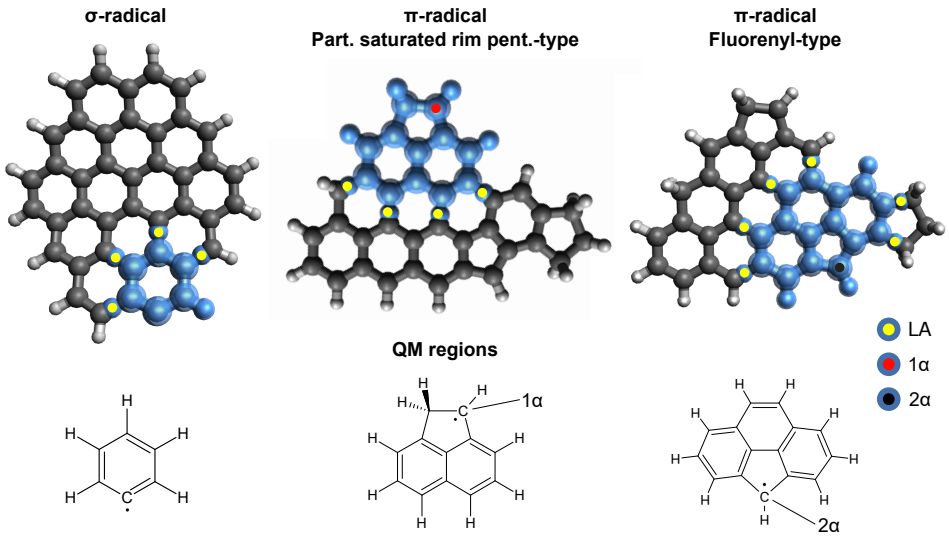

Figure S6: *Division of the system in a QM subsystem (blue) and an MM subsystem (gray) for the three type of radicals investigated in this work - σ-radical, partially saturated rim pentagon type π-radical (defined as $\mathbf{1}\alpha$ in Fig. 2g) and fluorenyl type π-radical (defined as $\mathbf{2}\alpha$ in Fig. 2g). Link atoms (LA) are introduced at the QM/MM boundary to cap the QM subsystem. The link atoms are present as a hydrogen atom in the QM calculation step.*

The interactions between the two subsystems are handled within the ONIOM approach by Morokuma and coworkers [32, 52]. In the ONIOM approach, the energy and gradients are first evaluated for the isolated QM subsystem at the desired level of *ab initio* theory. Subsequently, the energy and gradients of the total system, including the QM region, are computed using the molecular mechanics force field and added to the energy and gradients calculated for the isolated QM subsystems. Finally, in order to correct for counting the interactions inside the QM region twice, a molecular mechanics calculation is performed

on the isolated QM subsystem and the energy and gradients are subtracted. This leads to the following expression for the total QM/MM energy (and gradients likewise):

$$E_{\text{tot}} = E_{\text{I}}^{\text{QM}} + E_{\text{I+II}}^{\text{MM}} - E_{\text{I}}^{\text{MM}}, \tag{A.1}$$

where the subscripts I and II refers to the QM and MM subsystems, respectively. The superscripts indicate at what level of theory the energies are computed.

The sizes of the QM regions (see Fig. S6) have been selected to ensure an accurate electronic description of the reactive sites. This was firstly assumed looking at the similar values of the crosslink energy in 1,1',2,2'-Tetrahydro-1,1'-biacenaphthylene and 9,9'-Bifluorene [31, 33] and in bigger molecules presenting the same π-radical types, indicating that the QM regions selected are appropriate. The QM/MM method have been further benchmarked below:

- Calculation of crosslink energies: Geometry optimisations using the QM/MM method for the crosslinked molecules and monomers have been performed and crosslink energies have been calculated as the difference between the dimer energy and monomers energies (M06-2X/cc-pVTZ, which we have found to provide bond energies to within 4–8 kJ/mol [17, 58]). Energies of the bond between unstacked configurations of π-radicals (crosslinks between **1α-1α** sites, **2α-2α** sites and **1α-2α** sites as defined in Fig. 2g) were chosen as in the main text and are reported and compared with the electronic structure theory calculations in Fig. S7. We found that QM/MM method provide a similar energy to DFT with $\approx$ 10% of overbinding for the π-radical cases and $\approx$ 1.5% for the σ-radical case. The overestimation is mainly due to the lower level of theory used in the QM/MM simulations (M06-2X/def2-SVP) with respect to the electronic structure theory calculations (M06-2X/cc-pVTZ). We could not use the same level of theory due the high computational cost of the QM/MM simulations.

- Calculation of the intermolecular interactions between non-bonded stacked larger species: The dispersion interactions of two different stacked configurations have

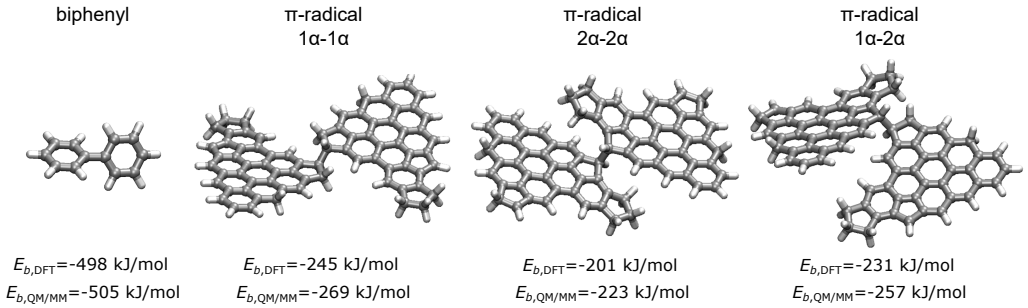

Figure S7: *Energies of the bond between phenyl radicals and between unstacked configurations of π-radicals (crosslinks between 1α-1α sites, 2α-2α sites and 1α-2α sites as defined in Fig. 2g) calculated using electronic structure theory calculations (M06-2X/cc-pVTZ) and QM/MM simulations (M06-2X/def2-SVP).*

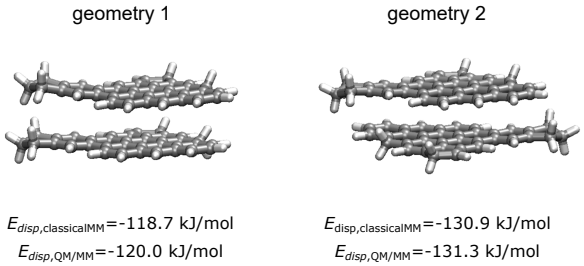

Figure S8: *Dispersion energies between non-bonded stacked larger species calculated using classical MM and QM/MM.*

been calculated using classical MM and QM/MM geometry optimisations (see Fig. S8). The values are in good agreement indicating that the QM/MM approach is able to treat the dispersion forces as well as the classical MM approach with the accurate isoPAHAP forcefield.

- Collision efficiency of phenyl recombination: The collision efficiency β is defined as the ratio of successful collisions (i.e. collisions which form dimers) to the total number of collisions. It is possible to estimate β from the MM/QM/MM simulations of radical-radical collisions as the fraction of effective collisions. We found 23 effective collisions over 1000 collisions for phenyl radicals at 1500 K, resulting in β equal to 0.023. It is important to mention that we have only considered direct collisions and we have not considered the collisions where the collision velocities are offset (impact factor) that would be required to accurately compute the collision efficiency. It is then more appropriate to refer to it as fraction of effective collisions. However, in case of small molecules, the impact factor for the offset collisions is small, so we do not expect a significant difference between the fraction of effective collisions and the collision efficiency for phenyl radical recombination.

  From the collision theory, the dimerization rate (r) of phenyl recombination can be expressed as:

$$r = k \cdot C_{\mathrm{PHE}}^2 = \beta \cdot \sqrt{\frac{4\pi k_b T}{m_{\mathrm{PHE}}}} \cdot d_{\mathrm{PHE}}^2 \cdot C_{\mathrm{PHE}}^2 \tag{A.2}$$

  where k is the rate constant, C_{PHE} is phenyl concentration, β is the collision efficiency, k_b is the Boltzmann constant, T is the temperature, m_{PHE} is the mass of the phenyl radical and d_{PHE} is the collision diameter expressed by:

$$d_{\mathrm{PHE}} = d_{\mathrm{A}} \sqrt{\frac{2n_{\mathrm{C}}}{3}} \tag{A.3}$$

  where d_A denotes the size of a single aromatic ring and equals to $1.395\sqrt{3}$ and n_c is the number of carbon atoms in the PAH monomer. It is then possible to calculate the collision efficiency β from the rate constant k:

$$\beta = \frac{k}{\sqrt{\frac{4\pi k_b T}{m_{\mathrm{PHE}}}} \cdot d_{\mathrm{PHE}}^2} \tag{A.4}$$

The collision efficiency for phenyl radical combinations ($\beta = 0.020$) derived using $k = 4 \cdot 10^{12}$ cm^3/mol/s taken from the high temperature shock tube study by Jin et al. [19] in Eq. A.4 is adopted for comparison. The two values are in reasonable agreement suggesting the results are comparable experimentally measured values for phenyl recombination.

A.4 Dimer dissociation lifetimes

Lifetimes for physical dimers were recorded using a distance cut-off of 2 nm between the monomers center of mass to distinguish between monomer and dimer state. The dissociation probability was defined as $N(t)/N(0)$, where $N(t)$ is the number of dimers that survived for at least t picoseconds and $N(0)$ is the initial number of dimers (in similar analysis to that performed by Chakraborty *et al.* [3]). In all the dissociation curves considered herein, there is an initial delay in the $N(t)/N(0)$ plots in which all the dimers survived. To fit the $N(t)/N(0)$ distributions versus time, we used a mono-exponential function of the following form:

$$\frac{N(t)}{N(0)} = -a \cdot \exp\left(\frac{1}{\tau} \cdot t\right) \tag{A.5}$$

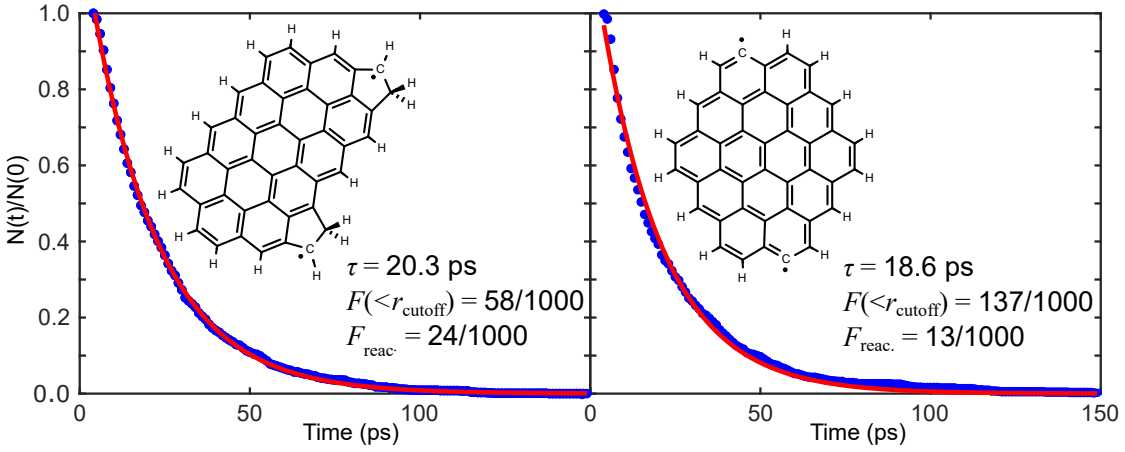

Figure S9: *Plots of $N(t)/N(0)$ and exponential fits for $M_2^* \rightarrow 2M$ dissociation a) M = IS22 and b) M = circumpyrene-2-nyl. The blue points represent the simulation results, whereas the red curves represent the exponential fit (Eq. A.5). Inset shows lifetimes, τ, fraction of reactive sites that approached the cutoff, $r_{\text{cutoff}} < 0.3$ and the fraction of effective collisions that go on to react, $F_{\text{reac.}}$*

The initial constant data points are not considered in the fitting. $N(t)/N(0)$ and the exponential fits are shown in Fig. S9.

τ is an indicator of the dimer dissociation lifetimes. As expected, τ increases with molecular mass being dependent on the dispersion force. Figure S10 shows that this trend is seen for all species where the dissociation time increases with molecular size while only for

the π-radicals a positive correlation is found between the fraction of effective collisions and the dissociation lifetime.

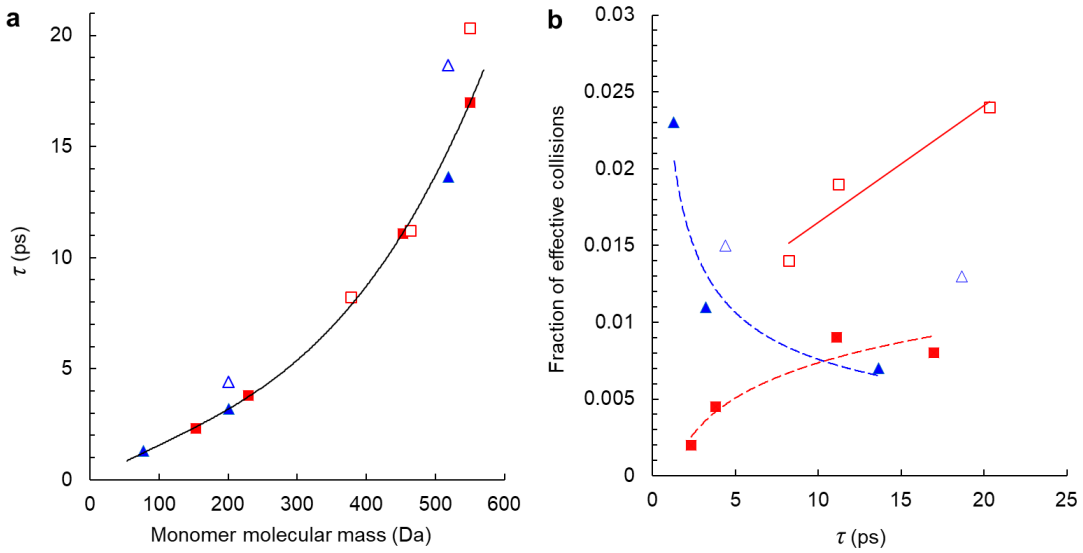

Figure S10: *a) dimer dissociation lifetimes (τ) versus monomer molecular mass and b) fraction of effective collisions versus dimer dissociation lifetimes (τ) for all the species investigated (Fig. 3 d-m): σ-monoradicals (filled triangles), σ-diradicals (open triangles), π-monoradicals (filled squares) and π-diradicals (open squares).*

References

[1] J. Abrahamson et al. Saturated platelets are new intermediates in hydrocarbon pyrolysis and carbon formation. *Nature*, 266(24):323–327, 1977. doi:10.1038/266323a0.

[2] T. C. Bond, S. J. Doherty, D. W. Fahey, P. M. Forster, T. Berntsen, B. J. Deangelo, M. G. Flanner, S. Ghan, B. Kärcher, D. Koch, S. Kinne, Y. Kondo, P. K. Quinn, M. C. Sarofim, M. G. Schultz, M. Schulz, C. Venkataraman, H. Zhang, S. Zhang, N. Bellouin, S. K. Guttikunda, P. K. Hopke, M. Z. Jacobson, J. W. Kaiser, Z. Klimont, U. Lohmann, J. P. Schwarz, D. Shindell, T. Storelvmo, S. G. Warren, and C. S. Zender. Bounding the role of black carbon in the climate system: A scientific assessment. *Journal of Geophysical Research Atmospheres*, 118(11):5380–5552, 2013. doi:10.1002/jgrd.50171.

[3] D. Chakraborty, H. Lischka, and W. L. Hase. Dynamics of pyrene-dimer association and ensuing pyrene-dimer dissociation. *The Journal of Physical Chemistry A*, 124 (43):8907–8917, 2020. doi:10.1021/acs.jpca.0c06677.

[4] P. Chen, S. Fatayer, B. Schuler, J. N. Metz, L. Gross, N. Yao, and Y. Zhang. The role of methyl groups in the early stage of thermal polymerization of polycyclic aromatic hydrocarbons revealed by molecular imaging. *Energy & Fuels*, page In Press, 2021. doi:10.1021/acs.energyfuels.0c04016.

[5] M. Commodo, K. Kaiser, G. De Falco, P. Minutolo, F. Schulz, A. D'Anna, and L. Gross. On the early stages of soot formation: Molecular structure elucidation by high-resolution atomic force microscopy. *Combustion and Flame*, 205:154–164, 2019. doi:10.1016/j.combustflame.2019.03.042.

[6] A. D'Anna, A. Violi, A. D'Alessio, and A. F. Sarofim. A reaction pathway for nanoparticle formation in rich premixed flames. *Combustion and Flame*, 127(1): 1995–2003, 2001. doi:10.1016/S0010-2180(01)00303-0.

[7] M. Frenklach and A. M. Mebel. On the mechanism of soot nucleation. *Physical Chemistry Chemical Physics*, 22(9):5314–5331, 2020. doi:10.1039/D0CP00116C.

[8] M. Frenklach and H. Wang. Detailed modeling of soot particle nucleation and growth. *Symposium (International) on Combustion*, 23(1):1559–1566, 1991. doi:10.1016/S0082-0784(06)80426-1.

[9] M. Frenklach, Z. Liu, R. I. Singh, G. R. Galimova, V. N. Azyazov, and A. M. Mebel. Detailed, sterically-resolved modeling of soot oxidation: Role of O atoms, interplay with particle nanostructure, and emergence of inner particle burning. *Combustion and Flame*, 188:284–306, 2018. doi:10.1016/j.combustflame.2017.10.012.

[10] M. J. Frisch, G. W. Trucks, H. B. Schlegel, G. E. Scuseria, M. A. Robb, J. R. Cheeseman, G. Scalmani, V. Barone, G. A. Petersson, H. Nakatsuji, X. Li, M. Caricato, A. V. Marenich, J. Bloino, B. G. Janesko, R. Gomperts, B. Mennucci, H. P. Hratchian, J. V. Ortiz, A. F. Izmaylov, J. L. Sonnenberg, D. Williams-Young, F. Ding,

F. Lipparini, F. Egidi, J. Goings, B. Peng, A. Petrone, T. Henderson, D. Ranasinghe, V. G. Zakrzewski, J. Gao, N. Rega, G. Zheng, W. Liang, M. Hada, M. Ehara, K. Toyota, R. Fukuda, J. Hasegawa, M. Ishida, T. Nakajima, Y. Honda, O. Kitao, H. Nakai, T. Vreven, K. Throssell, J. A. Montgomery, Jr., J. E. Peralta, F. Ogliaro, M. J. Bearpark, J. J. Heyd, E. N. Brothers, K. N. Kudin, V. N. Staroverov, T. A. Keith, R. Kobayashi, J. Normand, K. Raghavachari, A. P. Rendell, J. C. Burant, S. S. Iyengar, J. Tomasi, M. Cossi, J. M. Millam, M. Klene, C. Adamo, R. Cammi, J. W. Ochterski, R. L. Martin, K. Morokuma, O. Farkas, J. B. Foresman, and D. J. Fox. Gaussian~16 Revision B.01, 2016. Gaussian Inc. Wallingford CT.

[11] R. Ghafarian Shirazi, F. Neese, and D. A. Pantazis. Accurate spin-state energetics for aryl carbenes. *Journal of chemical theory and computation*, 14(9):4733–4746, 2018.

[12] F. J. Giessibl. High-speed force sensor for force microscopy and profilometry utilizing a quartz tuning fork. *Applied Physics Letters*, 73(26):3956–3958, 1998. doi:10.1063/1.122948.

[13] L. Gross, F. Mohn, N. Moll, P. Liljeroth, and G. Meyer. The chemical structure of a molecule resolved by atomic force microscopy. *Science*, 325(5944):1110–1114, 2009. doi:10.1126/science.1176210.

[14] L. Gross, N. Moll, F. Mohn, A. Curioni, G. Meyer, F. Hanke, and M. Persson. High-resolution molecular orbital imaging using a p-wave stm tip. *Physical Review Letters*, 107(8):086101, 2011.

[15] N. Hansen, T. A. Cool, P. R. Westmoreland, and K. Kohse-Höinghaus. Recent contributions of flame-sampling molecular-beam mass spectrometry to a fundamental understanding of combustion chemistry. *Progress in Energy and Combustion Science*, 35(2):168–191, 2009. doi:10.1016/j.pecs.2008.10.001.

[16] S. J. Harris and A. M. Weiner. A picture of soot particle inception. *Symposium (International) on Combustion*, 22(1):333 – 342, 1989. doi:10.1016/S0082-0784(89)80039-6.

[17] D. Hou and X. You. Reaction kinetics of hydrogen abstraction from polycyclic aromatic hydrocarbons by H atoms. *Physical Chemistry Chemical Physics*, 19(45): 30772–30780, 2017. doi:10.1039/c7cp04964a.

[18] A. Issaris, D. Vanderzande, and J. Gelan. Polymerization of a p-quinodimethane derivative to a precursor of poly (p-phenylene vinylene)—indications for a free radical mechanism. *Polymer*, 38(10):2571–2574, 1997. doi:10.1016/S0032-3861(96)00468-5.

[19] H. Jin, B. R. Giri, D. Liu, and A. Farooq. A high temperature shock tube study of phenyl recombination reaction using laser absorption spectroscopy. *Proc. Combust. Instit.*, In Press, 2020. doi:10.1016/j.proci.2020.06.164.

[20] K. Johansson, M. Head-Gordon, P. Schrader, K. Wilson, and H. Michelsen. Resonance-stabilized hydrocarbon-radical chain reactions may explain soot inception and growth. *Science*, 361(6406):997–1000, 2018. doi:10.1126/science.aat3417.

[21] M. R. Kholghy, G. A. Kelesidis, and S. E. Pratsinis. Reactive polycyclic aromatic hydrocarbon dimerization drives soot nucleation. *Physical Chemistry Chemical Physics*, 20:10926–10938, 2018. doi:10.1039/C7CP07803J.

[22] D. Kittelson and M. Kraft. Particle formation and models. *Encyclopedia of Automotive Engineering*, pages 1–23, 2014.

[23] D. Koley, E. Arunan, and S. Ramakrishnan. Computational investigations on covalent dimerization/oligomerization of polyacenes: Is it relevant to soot formation? *Journal of Computational Chemistry*, 33(21):1762–1772, 2012. doi:10.1002/jcc.23014.

[24] P. J. Landrigan, R. Fuller, N. J. Acosta, O. Adeyi, R. Arnold, A. B. Baldé, R. Bertollini, S. Bose-O'Reilly, J. I. Boufford, P. N. Breysse, et al. The lancet commission on pollution and health. *The lancet*, 391(10119):462–512, 2018. doi:10.1016/S0140-6736(17)32345-0.

[25] P. Lavvas, M. Sander, M. Kraft, and H. Imanaka. Surface chemistry and particle shape: processes for the evolution of aerosols in titan's atmosphere. *The Astrophysical Journal*, 728(2):80, 2011. doi:10.1088/0004-637X/728/2/80.

[26] J. Li, S. Sanz, J. Castro-Esteban, M. Vilas-Varela, N. Friedrich, T. Frederiksen, D. Peña, and J. I. Pascual. Uncovering the triplet ground state of triangular graphene nanoflakes engineered with atomic precision on a metal surface. *Physical Review Letters*, 124(17):177201, 2020. doi:10.1103/PhysRevLett.124.177201.

[27] F. Lombardi, W. K. Myers, J. Ma, J. Liu, X. Feng, and L. Bogani. Dynamical nuclear decoupling of electron spins in molecular graphenoid radicals and biradicals. *Physical Review B*, 101(9):094406, 2020. doi:10.1103/PhysRevB.101.094406.

[28] K. Luther, K. Oum, K. Sekiguchi, and J. Troe. Recombination of benzyl radicals: dependence on the bath gas, temperature, and pressure. *Physical Chemistry Chemical Physics*, 6(16):4133–4141, 2004. doi:10.1039/B407074G.

[29] Q. Mao, D. Hou, K. H. Luo, and X. You. Dimerization of polycyclic aromatic hydrocarbon molecules and radicals under flame conditions. *The Journal of Physical Chemistry A*, 122(44):8701–8708, 2018. doi:10.1021/acs.jpca.8b07102.

[30] J. W. Martin, M. Botero, R. I. Slavchov, K. Bowal, J. Akroyd, S. Mosbach, and M. Kraft. Flexoelectricity and the formation of carbon nanoparticles in flames. *The Journal of Physical Chemistry C*, 122(38):22210–22215, 2018. doi:10.1021/acs.jpcc.8b08264.

[31] J. W. Martin, D. Hou, A. Menon, L. Pascazio, J. Akroyd, X. You, and M. Kraft. Reactivity of polycyclic aromatic hydrocarbon soot precursors: Implications of localized π-radicals on rim-based pentagonal rings. *The Journal of Physical Chemistry C*, 123(43):26673–26682, 2019. doi:10.1021/acs.jpcc.9b07558.

[32] F. Maseras and K. Morokuma. IMOMM: A new ab initio + molecular mechanics geometry optimization scheme of equilibrium structures and transition states. *J. Comp. Chem.*, 16:1170–1179, 1995. doi:10.1002/jcc.540160911.

[33] A. Menon, J. W. Martin, J. Akroyd, and M. Kraft. Reactivity of polycyclic aromatic hydrocarbon soot precursors: Kinetics and equilibria. *The Journal of Physical Chemistry A*, 2020. doi:10.1021/acs.jpcc.9b07558.

[34] A. Menon, J. W. Martin, G. Leon, D. Hou, L. Pascazio, X. You, and M. Kraft. Reactive localized π-radicals on rim-based pentagonal rings: properties and concentration in flames. *Proceedings of the Combustion Institute*, In Press, 2020. doi:10.1016/j.proci.2020.07.042.

[35] H. A. Michelsen. Probing soot formation, chemical and physical evolution, and oxidation: A review of in situ diagnostic techniques and needs. *Proceedings of the Combustion Institute*, 36(1):717–735, 2017. doi:10.1016/j.proci.2016.08.027.

[36] J. H. Miller. The kinetics of polynuclear aromatic hydrocarbon agglomeration in flames. *Symposium (International) on Combustion*, 23(1):91 – 98, 1991. doi:10.1016/S0082-0784(06)80246-8.

[37] S. Mishra, D. Beyer, K. Eimre, S. Kezilebieke, R. Berger, O. Gröning, C. A. Pignedoli, K. Müllen, P. Liljeroth, P. Ruffieux, et al. Topological frustration induces unconventional magnetism in a nanographene. *Nature nanotechnology*, 15 (1):22–28, 2020. doi:10.1038/s41565-019-0577-9.

[38] Z. Mou, K. Uchida, T. Kubo, and M. Kertesz. Evidence of σ-and π-dimerization in a series of phenalenyls. *Journal of the American Chemical Society*, 136(52):18009–18022, 2014. doi:10.1021/ja509243p.

[39] F. Neese. The orca program system. *Wiley Interdisciplinary Reviews: Computational Molecular Science*, 2(1):73–78, 2012. doi:10.1002/wcms.81.

[40] M. Pelucchi, C. Cavallotti, T. Faravelli, and S. Klippenstein. H-abstraction reactions by oh, ho_2, o, o_2 and benzyl radical addition to o_2 and their implications for kinetic modelling of toluene oxidation. *Physical Chemistry Chemical Physics*, 20 (16):10607–10627, 2018. doi:10.1039/C7CP07779C.

[41] T. Pino, G. Féraud, P. Bréchignac, E. J. Bieske, and T. W. Schmidt. Laboratory spectroscopy of PAHs. *Proceedings of the International Astronomical Union*, 9 (S297):247–257, 2013. doi:10.1017/S1743921313015950.

[42] J. Repp, G. Meyer, S. M. Stojković, A. Gourdon, and C. Joachim. Molecules on insulating films: scanning-tunneling microscopy imaging of individual molecular orbitals. *Physical Review Letters*, 94(2):026803, 2005.

[43] D. Rodríguez-Urrego and L. Rodríguez-Urrego. Air quality during the covid-19: Pm2. 5 analysis in the 50 most polluted capital cities in the world. *Environmental Pollution*, page 115042, 2020. doi:10.1016/j.envpol.2020.115042.

[44] H. Sabbah, M. Commodo, F. Picca, G. De Falco, P. Minutolo, A. D'Anna, and C. Joblin. Molecular content of nascent soot: Family characterization using two-step laser desorption laser ionization mass spectrometry. *Proceedings of the Combustion Institute*, 2020. doi:10.1016/j.proci.2020.09.022.

[45] B. Schuler, W. Liu, A. Tkatchenko, N. Moll, G. Meyer, A. Mistry, D. Fox, and L. Gross. Adsorption geometry determination of single molecules by atomic force microscopy. *Physical review letters*, 111(10):106103, 2013.

[46] B. Schuler, Y. Zhang, S. Collazos, S. Fatayer, G. Meyer, D. Pérez, E. Guitián, M. R. Harper, J. D. Kushnerick, D. Pena, et al. Characterizing aliphatic moieties in hydrocarbons with atomic force microscopy. *Chemical science*, 8(3):2315–2320, 2017.

[47] F. Schulz, M. Commodo, K. Kaiser, G. D. Falco, P. Minutolo, G. Meyer, A. D'Anna, and L. Gross. Insights into incipient soot formation by atomic force microscopy. *Proceedings of the Combustion Institute*, 37(1):885 – 892, 2019. doi:10.1016/j.proci.2018.06.100.

[48] M. Solà. Forty years of clar's aromatic π-sextet rule. *Frontiers in chemistry*, 1:22, 2013.

[49] T. Stuyver, B. Chen, T. Zeng, P. Geerlings, F. De Proft, and R. Hoffmann. Do diradicals behave like radicals? *Chemical reviews*, 119(21):11291–11351, 2019. doi:10.1021/acs.chemrev.9b00260.

[50] X. Su, C. Li, Q. Du, K. Tao, S. Wang, and P. Yu. Atomically precise synthesis and characterization of heptauthrene with triplet ground state. *Nano letters*, 20(9): 6859–6864, 2020. doi:10.1021/acs.nanolett.0c02939.

[51] W. Sun, X. Gao, B. Wu, and T. Ombrello. The effect of ozone addition on combustion: Kinetics and dynamics. *Progress in Energy and Combustion Science*, 73:1–25, 2019. doi:10.1016/j.pecs.2019.02.002.

[52] M. Svensson, S. Humbel, R. Froes, T. Matsubara, S. Sieber, and K. Morokuma. ONIOM a multilayered integrated MO + MM method for geometry optimizations and single point energy predictions. a test for Diels-Alder reactions and Pt(P(t-Bu)3)2 + H2 oxidative addition. *J. Phys. Chem.*, 100:19357, 1996. doi:10.1021/jp962071j.

[53] T. S. Totton, A. J. Misquitta, and M. Kraft. A quantitative study of the clustering of polycyclic aromatic hydrocarbons at high temperatures. *Physical Chemistry Chemical Physics*, 14(12):4081–94, 2012. doi:10.1039/c2cp23008a.

[54] G. Vitiello, G. De Falco, F. Picca, M. Commodo, G. D'Errico, P. Minutolo, and A. D'Anna. Role of radicals in carbon clustering and soot inception: A combined EPR and raman spectroscopic study. *Combustion and Flame*, 205:286–294, 2019. doi:10.1016/j.combustflame.2019.04.028.

[55] H. Wang. Formation of nascent soot and other condensed-phase materials in flames. *Proceedings of the Combustion Institute*, 33(1):41–67, 2011. doi:10.1016/j.proci.2010.09.009.

[56] X. Wu, R. Nethery, M. Sabath, D. Braun, and F. Dominici. Air pollution and covid-19 mortality in the united states: Strengths and limitations of an ecological regression analysis. *Science advances*, 6(45):eabd4049, 2020. doi:10.1126/sciadv.abd4049.

[57] H. B. Zhang, X. You, H. Wang, and C. K. Law. Dimerization of polycyclic aromatic hydrocarbons in soot nucleation. *The Journal of Physical Chemistry A*, 118(8): 1287–1292, 2014. doi:10.1021/jp411806q.

[58] Y. Zhao and D. G. Truhlar. The m06 suite of density functionals for main group thermochemistry, thermochemical kinetics, noncovalent interactions, excited states, and transition elements: two new functionals and systematic testing of four m06-class functionals and 12 other functionals. *Theoretical Chemistry Accounts*, 120 (1-3):215–241, 2008. doi:10.1007/s00214-007-0310-x.